Supplementary Information

Concerted Electron-Nuclear Motion in Proton-Coupled Electron Transfer (PCET)-Driven Grotthuss-Type Proton Translocation

Eric A. Arsenault,[1,2,3†] Walter D. Guerra,[4†] James Shee,[1,5†] Edgar A. Reyes Cruz,[4,6†] Yusuke Yoneda,[1,2,3,7] Brian L. Wadsworth,[4,6] Emmanuel Odella,[4] Maria N. Urrutia,[4] Gerdenis Kodis,[4,6] Gary F. Moore,[4,6] Martin Head-Gordon,[1,5] Ana L. Moore,[4] Thomas A. Moore,[4] and Graham R. Fleming[1,2,3]*

[1]Department of Chemistry, University of California, Berkeley, CA 94720, USA
[2]Molecular Biophysics and Integrated Bioimaging Division, Lawrence Berkeley National Laboratory, Berkeley, CA 94720, USA
[3]Kavli Energy Nanoscience Institute at Berkeley, Berkeley, CA 94720, USA
[4]School of Molecular Sciences, Arizona State University, Tempe, AZ 85287, USA
[5]Chemical Sciences Division, Lawrence Berkeley National Laboratory, Berkeley, CA 94720, USA
[6]The Biodesign Institute Center for Applied Structural Discovery (CASD), Tempe, AZ 85287, USA
[7]Present Address: Research Center of Integrative Molecular Systems, Institute for Molecular Science, National Institute of Natural Sciences, Okazaki, Aichi, 444-8585, Japan
[†]These authors contributed equally
*Email: grfleming@lbl.gov

Table of Contents

1. METHODS…...……...…….…S3

1.1 Synthesis...……..……S3

1.2 Infrared Spectroelectrochemistry (IRSEC)……..……...S3

1.3 Cyclic Voltammetry……..…….....S4

1.4 Two-Dimensional Electronic-Vibrational (2DEV) Spectroscopy…….…….……S4

1.5 Electronic Structure Calculations...……..…..…….……...……S6

2. EXPERIMENTAL RESULTS…..……S7

2.1 Electrochemical Characterization……...S7

2.2 Absorption Spectrum.……S8

2.3 Center Line Slope (CLS) Analysis…….....S9

2.4 Excitation Frequency Peak EvolutionAnalysis……...……...S9

3. COMPUTATIONAL RESULTS..…….……S11

4. REFERENCES……..……..S17

1. METHODS

1.1 Synthesis

Synthesis of (2-(*tert*-butyl)-6-(7-(4-methoxypyridin-2-yl)-1*H*-benzo[*d*]imidazol-2-yl)-4-(10,15,20-tris(perfluorophenyl)porphyrin-5-yl)-phenol, PF_{15}-BIP-Pyr) was performed following previously reported methodology.[1] Design, procedures, and characterization were described in the same report.

1.2 Infrared Spectroelectrochemistry (IRSEC)

IRSEC measurements were conducted using a Biologic SP200 potentiostat connected to an optically transparent thin-layer electrochemical cell (Spectroelectrochemistry Reading RT OTTLE cell) equipped with CaF_2 optical windows. The cell (pathlength 0.2 mm) contained a Pt mesh counter electrode, a Ag wire pseudoreference electrode, and a Pt mesh working electrode, which was positioned in the light path of the IR spectrophotometer (Bruker Vertex 70 spectrometer, GloBar MIR source, broadband KBr beamsplitter, and liquid nitrogen cooled MCT detector). For all IRSEC measurements, the compounds were used at a concentration of ~5 mM, with 0.1 M tetrabutylammonium hexafluorophosphate ($TBAPF_6$) as the supporting electrolyte in deuterated acetonitrile or chloroform, and the cell was sealed under an argon atmosphere. Thin-layer constant potential electrolysis was monitored via FTIR as the working electrode was polarized in 100 and 50 mV increments versus the silver wire reference. Absorption spectra (64 scans, 2 cm^{-1} resolution) were continuously collected at each applied potential until there were no further significant changes. This procedure was conducted in a similar fashion as previously reported measurements.[2,3]

1.3 Cyclic Voltammetry

Cyclic voltammetry measurements were performed with a Biologic SP200 potentiostat using a glassy carbon (3 mm diameter) working electrode, a Pt wire counter electrode, and a Ag wire pseudo-reference electrode in a conventional three-electrode cell. These measurements were collected at room temperature in anhydrous acetonitrile containing the compound of interest at a concentration of 1 mM and under an argon atmosphere. 0.5 M $TBAPF_6$ acetonitrile was used as the supporting electrolyte, and the scan rate was 100 mV s^{-1}. The working electrode was cleaned between experiments by polishing with a 0.05 μm alumina slurry on a microcloth pad, followed by solvent rinses and drying under a stream of nitrogen. The potential of the pseudoreference electrode was determined using the ferrocenium/ferrocene redox couple as an internal standard and adjusting to the saturated calomel electrode (SCE) scale (with $E_{1/2}$ taken to be 0.40 V versus SCE in acetonitrile).[4]

1.4 Two-Dimensional Electronic-Vibrational Spectroscopy

A detailed description for the two-dimensional electronic-vibrational (2DEV) spectroscopic setup can be found elsewhere.[5] Briefly, the output of a Ti:sapphire oscillator (Vitara-S, Coherent) was regeneratively amplified with a 1 kHz repetition rate (Legend Elite, Coherent), an energy of 1 mJ/pulse, and a pulse duration of 40 fs. The amplified pulse was divided into two and one was used to pump a home-built visible non-collinear optical parametric amplifier (NOPA). The other pulse was used to generate a mid-IR probe pulse (centered at 6.2 μm) by difference frequency generation with signal and idler pulses from a near-IR collinear OPA. The output of the NOPA (centered at 580 nm, 60 nm fwhm) was compressed to 10 fs at the sample position using a pair of prisms and an acousto-optic dispersive programmable filter (AODPF, Dazzler, Fastlite). The pulse pair was introduced to a retroreflector on a motorized translation stage

to control the waiting time, T, between the pump and probe pulses. The total power of the pump pulses was 200 nJ and the pulses were focused into the sample with spot size of 250 μm. The mid-IR pulse was divided by a 50:50 beam splitter to form probe and reference beams. The probe and reference beams were dispersed by a spectrometer (Horiba, Triax 180) and detected by a 64-pixel HgCdTe dual array (Infrared Systems Development). The cross-correlation between visible and mid-IR pulses was estimated to be 90 fs by a step-like transient IR response of a 50 μm Ge plate and by a solvent only measurement. See Figure S1.

For each waiting time, a 2DEV spectrum was acquired by using the AODPF to scan the t_1 delay over 0-100 fs with 2.5 fs steps. For each t_1 delay, the signal was acquired with the relative phase between the pump pulses φ_{12} set by 0, $2\pi/3$ and $4\pi/3$, and the desired signal was isolated by a 3×1 phase cycling scheme.[6,7] The excitation axis was obtained by a Fourier transformation over t_1. The signal was collected in the fully rotated frame with respect to t_1.

The CLS (see Figure 3b in main text and Figure S4) was calculated by linear fitting of the conditional averages along visible axis[8] as the CLS along the IR axis reflects the same information.[9] Excitation frequency peak evolution (see Figure 3a in main text and Figure S5-S7) was calculated by fitting the 2DEV spectrum along visible excitation axis at a particular IR probe frequency at each waiting time with a Gaussian function.

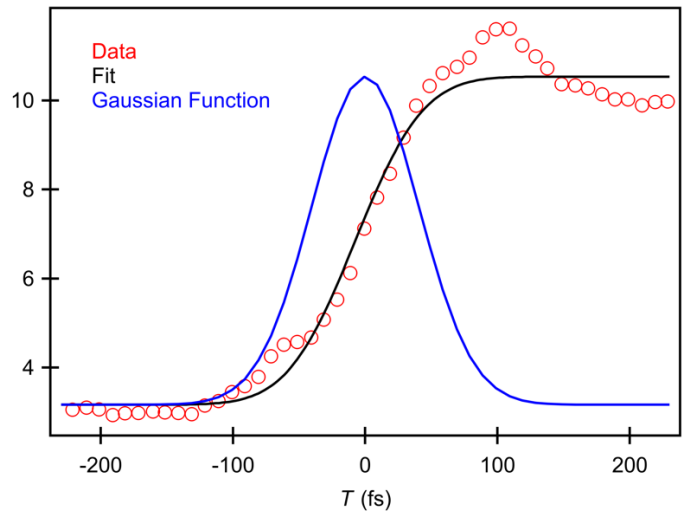

Figure S1. The instrument function for 2DEV spectra is determined by measuring the rise of the visible pump IR probe signal from a 50 nm Ge plate and fitting the rise to a Gaussian resulting in a FWHM of 95 fs.

1.5 Electronic Structure Calculations

All geometries (both ground and excited states) were optimized with the PBE0 functional[10] and the def2-SV(P) basis set. To investigate the evolution of the dipole moment as a function of dihedral angle, we performed constrained optimizations in which the dihedral angle is fixed to specified values while all other degrees of freedom are allowed to relax.

Excited state properties such as dipole moments were modeled with linear-response time-dependent density functional theory (TDDFT)[11] using the LRC-ωPBEh functional, with the original choice of range separation parameter (ω=0.2).[12] For energetic quantities, the range separation parameter was optimally tuned[13] with respect to the E2PT state with 90° dihedral twist, resulting in ω=0.109. The LRC-ωPBEh functional thus specified was used for all geometries and electronic states for consistency in relative energy predictions.

All calculations were performed with the Q-Chem software package[14], and used the conductor-like polarizable continuum model to model[15] the electrostatics due to the acetonitrile solvent. We used a dielectric constant of 35.9, Bondi radii, the Switching/Gaussian method for surface discretization, and default settings for all other model parameters.

2. EXPERIMENTAL RESULTS

2.1 Electrochemical Characterization

The free energy gap ΔG was estimated by the Rehm-Weller equation[16,17]

$$\Delta G = -E_{00} + E_{1/2}(\mathrm{PF_{15}\text{-}BIP\text{-}Py^{+}/\ PF_{15}\text{-}BIP\text{-}Py}) - E_{1/2}(\mathrm{PF_{15}\text{-}BIP\text{-}Py/\ PF_{15}\text{-}BIP\text{-}Py^{-}}) - \frac{e^2}{4\pi\varepsilon_0\varepsilon_s l}$$

where E_{00} is an energy difference between S_0 and S_1 states, $E_{1/2}$(PF_{15}-BIP-Py^+/PF_{15}-BIP-Py) and $E_{1/2}$(PF_{15}-BIP-Py/PF_{15}-BIP-Py^-) are midpoint potentials for the PF_{15}-BIP-Py^+/PF_{15}-BIP-Py and PF_{15}-BIP-Py/PF_{15}-BIP-Py^- redox couples, e is the elementary charge, ε_0 is the permittivity of vacuum, ε_s is a dielectric constant of the solvent, and l is a distance between donor and acceptor molecules. According to the equation, the free energy gap for E2PT product was estimated to be ΔG = -300 meV. The parameters used for the estimation of ΔG are summarized in Table S1.

For the E1PT product, ΔG was estimated based on Table 2 of Ref. 18.

Table S1. Parameters used for the estimation of ΔG for E2PT.

E_{00} (eV)	E_{ox} (eV)	E_{red} (eV)	ε_s[19]	l (Å)
1.92	0.93	-0.83	36.6	6.4

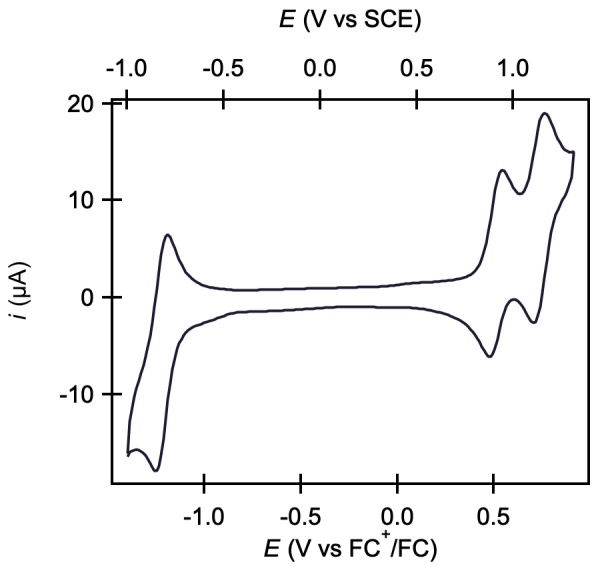

Figure S2. Cyclic voltammetry of PF_{15}-BIP-Py. The midpoint potentials ($E_{1/2}$) for the PF_{15}-BIP-Py^+/PF_{15}-BIP-Py and PF_{15}-BIP-Py/PF_{15}-BIP-Py^- redox couples were estimated as the average of the anodic and cathodic peak potentials, yielding values of +0.85 and -0.83 V versus SCE, respectively.

2.2 Absorption Spectrum

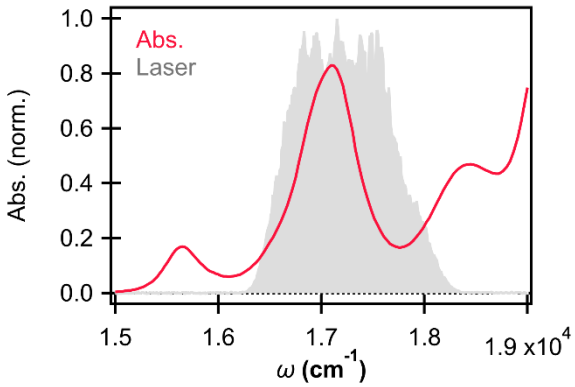

Figure S3. Normalized electronic absorption spectrum of PF_{15}-BIP-Pyr (red). The spectrum of the excitation laser pulse is also shown (gray).

2.3 Center Line Slope (CLS) Analysis

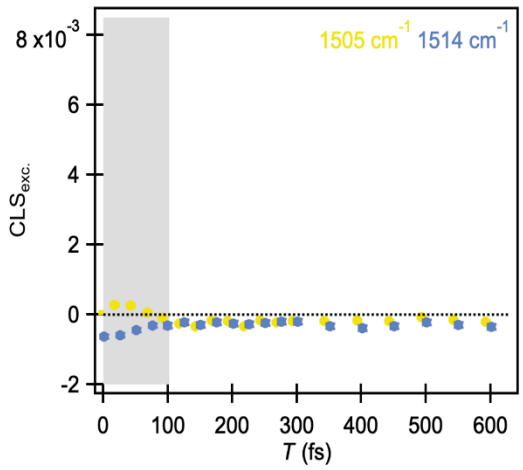

Figure S4. CLS dynamics of PF_{15}-BIP-Py for features unrelated to the BIP-Py (*i.e.*, localized on PF_{15}).[20] The time range where visible and IR pulses overlap, <90 fs, is indicated by the gray area. The error bars indicated the standard error of the CLS, obtained by a linear fit of the conditional average.[8] A comparison to Figure 3b in the main text reveals a distinct lack of oscillatory (or any) dynamics for these features which are unrelated to the E2PT product.

2.4 Excitation Frequency Peak Evolution Analysis

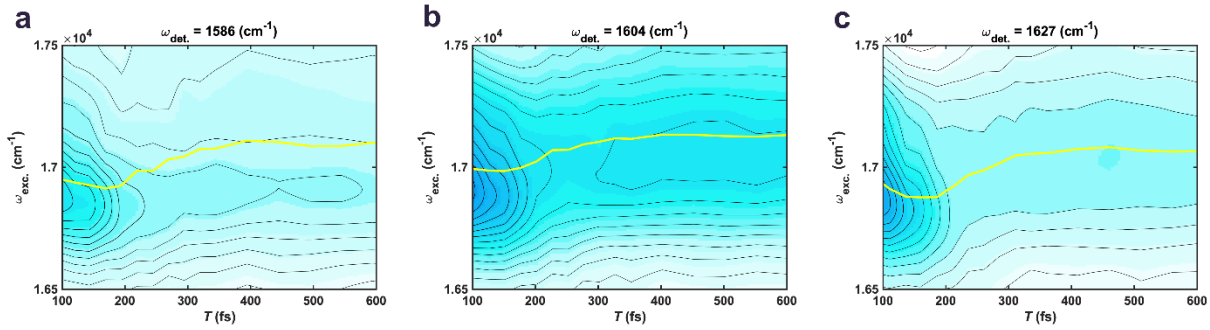

Figure S5. $\omega_{exc.}$ peak evolution of PF_{15}-BIP-Pyr at 1586 cm^{-1}, 1604 cm^{-1}, and 1627 cm^{-1} corresponding to Figure 3a in the main text. The yellow line traces the peak maximum along the waiting time, *T*, obtained by fitting with a Gaussian function.

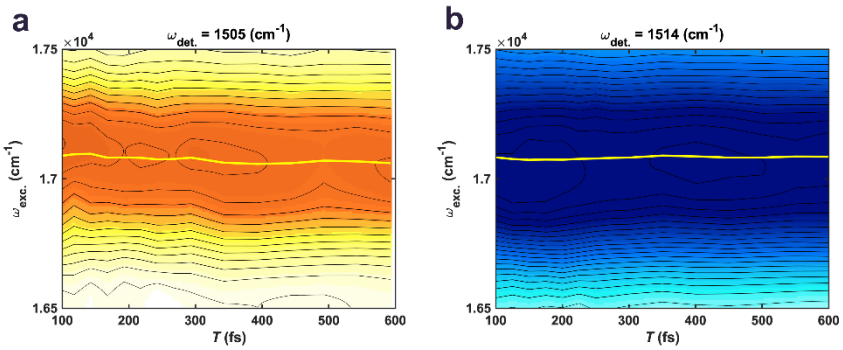

Figure S6. $\omega_{exc.}$ peak evolution of PF_{15}-BIP-Pyr for features unrelated to the BIP-Py (*i.e.*, localized on PF_{15}) at 1505 cm^{-1} and 1514 cm^{-1}.[20] The yellow line traces the peak maximum along the waiting time, *T*, obtained by fitting with a Gaussian function.

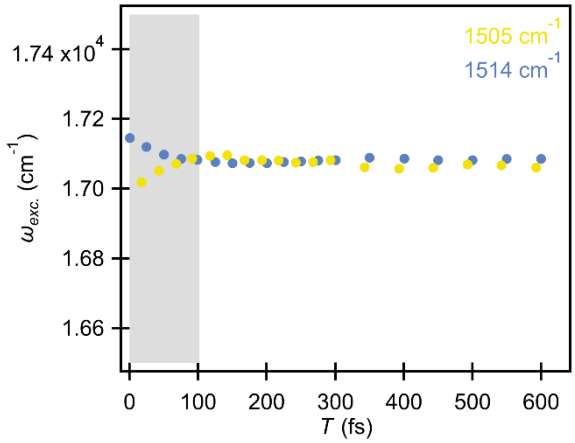

Figure S7. $\omega_{exc.}$ peak evolution of PF_{15}-BIP-Pyr for features unrelated to the BIP-Py (i.e. localized on PF_{15}) at 1505 cm^{-1} and 1514 cm^{-1}.[20] The time range where visible and IR pulses overlap, <90 fs, is indicated by the shaded area. A comparison to Figure 3a in the main text reveals a distinct lack of oscillatory (or any) dynamics for these features which are unrelated to the E2PT product.

3. COMPUTATIONAL RESULTS

The ground state dihedral angle was predicted to be 63.0°, using the PBE0 functional (68° when optimized with the LRC-ωPBEh functional).

The excited-state dipole moments as a function of dihedral angle are shown in Figure S7. We include the original LRC-ωPBEh functional, in addition to an optimally tuned variant, to enable comparisons with the single proton-transfer system from our prior work.[20]

The ground-state dipole moment was calculated to be 8.62 D with the LRC-ωPBEh functional, and 8.67 D with the tuned range separation parameter.

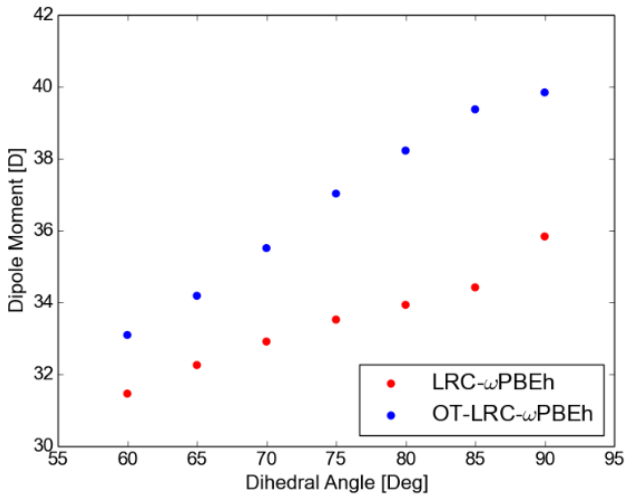

Figure S8. Dipole moment as a function of phenol-porphyrin dihedral angle. Predictions of the unaltered LRC-ωPBEh functional are shown red, while the results from the optimally tuned functional (ω=0.109) with respect to the E2PT geometry with the 90° dihedral angle are shown in blue.

Natural transition orbitals[21] are shown in Figures S9 and S10, corresponding to 60° and 90° dihedral twist angles. The extent of charge-transfer is seen to increase with twist angle, which is consistent with the increasing dipole moments.

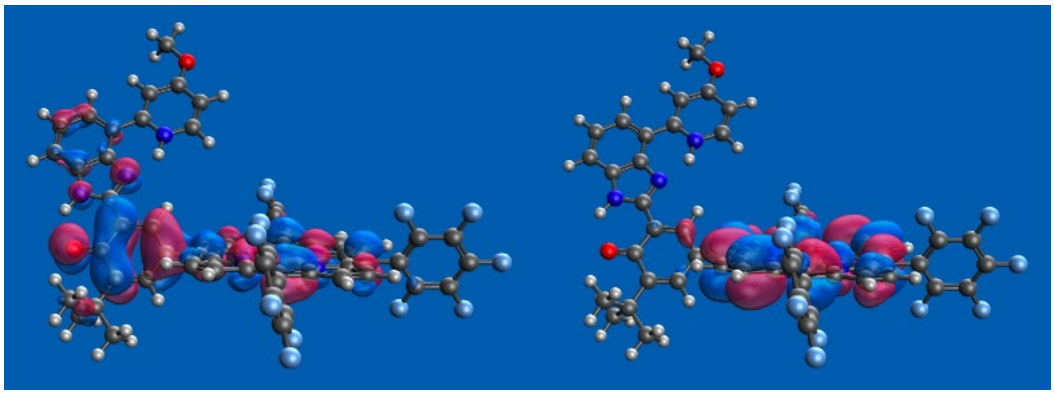

Figure S9. Natural transition orbitals (NTOs) at 60° dihedral twist, from the OT-LRC-ωPBEh functional. The left/right plot shows the hole/electron NTOs.

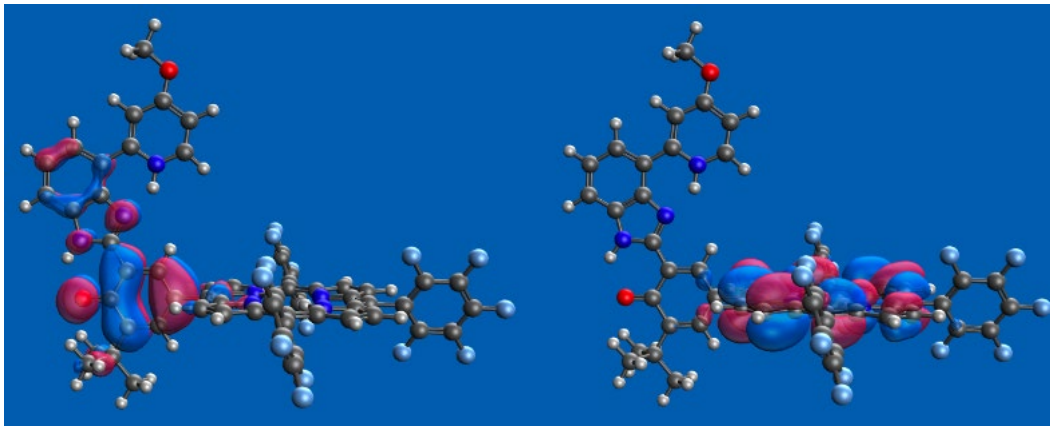

Figure S10. Natural transition orbitals (NTOs) at 60° dihedral twist, from the OT-LRC-ωPBEh functional. The left/right plot shows the hole/electron NTOs.

Quantitative computational comparisons of the relative energetics between the LE state and charge-transfer states with large excited state dipole moments (*e.g.*, E1PT and E2PT) in polar solvents are not possible due to previously studied limitations of implicit solvation models.[13] Furthermore, we found that the qualitative shapes of E1PT and E2PT energy surfaces are sensitive to the density functional employed (LRC-ωPBEh with ω=0.2 predicts that E1PT and E2PT energies are lowered when twisting from 60° to 90°, while ω=0.109 finds that the energies increase). As a result, we do not attempt to compare differences between the LE state and either the E1PT or E2PT states. However, as the dipole moments of the E1PT and E2PT states are both relatively large, predictions of the energy difference between the two ought to be reasonably accurate due to a substantial (but perhaps not complete) cancellation of the errors due to the implicit solvation model, and accurate gas-phase energetics from the optimally tuned range-separated hybrid functional.

As shown in Table S2, the various predictions (over a range of dihedral angles) are in agreement with the experimental finding that the E1PT state is higher in energy than the E2PT state. The estimate based on electrochemical measurements is 160 meV (see Section 2.1), in reasonable agreement with our calculated range.

In addition, we note that the total energy of the LE state in the Franck-Condon region is -4367.1584 Hartrees. At a comparable dihedral angle (65°) and after a constrained optimization of the E2PT state in implicit solvent, the total energy of the E2PT state is -4367.1611 Hartrees, *i.e.*, ~72 meV lower than the initially populated LE. Of course, implicit solvent models have been shown to put charge-transfer excitation energies in acetonitrile artificially high in energy by >300 meV[13], and so we can be confident that after double proton transfer and at a similar twist angle to the ground-state, the E2PT state is exergonic versus the FC LE state.

Table S2. Calculated energy differences [meV] between the E1PT and E2PT states (*i.e.*, E1PT - E2PT), as predicted with the tuned LRC-ωPBEh functional in implicit acetonitrile solvent. The experimental estimate, from electrochemical measurements, is 160 meV.

Dihedral [deg]	ΔE(LRC-ωPBEh) [meV]	ΔE(OT-LRC-ωPBEh) [meV]
60	111	88
65	128	98
70	141	112
75	150	133
80	161	157
85	174	184
90	184	220

Finally, the fraction of charge transfer (CT) from the BIP to the porphyrin at a dihedral similar to that in the FC region has, in our prior work, been estimated to be roughly 0.50 (50%). This was obtained by comparing the change in calculated dipole moment (going from the ground-state to the charge-separated excited state) to the maximum increase, $\Delta\mu_{max}$, implied by a point charge model, *i.e.*, an electron and a hole with charge magnitudes, Q, that evolve from 0 to 1.6×10^{-19} C, separated by R_{eh} = 6.4 Å. At this separation $\Delta\mu_{max}$ = 30.7 D, and we can write

$$frac\ CT = \frac{Q_{ES} - Q_{GS}}{\Delta Q_{max}} = \frac{Q_{ES}R_{eh} - Q_{GS}R_{eh}}{\Delta Q_{max}R_{eh}} \approx \frac{\mu_{ES} - \mu_{GS}}{\Delta\mu_{max}}$$

where ES and GS stand for excited-state and ground-state, respectively, and the last equality is approximate given that the dipole moments in the numerator on the right-hand-side, which were calculated from *ab initio* electron densities, are mapped to the separated point charge model.

In the present work investigating the E2PT state, at a dihedral angle of 60°, μ_{ES} = 31.5 D and μ_{GS} = 8.6 D. The fraction of CT, as presented in the main text, is 75%.

In Figure S11, the fraction of CT is plotted as a function of dihedral angle in the E2PT state. The optimally tuned LRC-ωPBEh functional predicts that at an angle similar to that in the GS, 80% of the CT has already occurred. Twisting from 60° to 90° completes the CT processes. We also show results from the previously parameterized LRC-ωPBEh functional, to enable a comparison with our previous work.

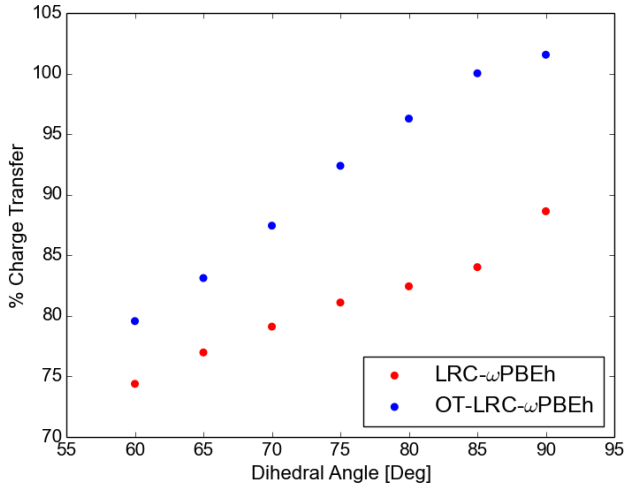

Figure S11. Percentage of CT as a function of dihedral angle [deg], with the originally and optimally tuned LRC-ωPBEh functional.

4. REFERENCES

(1) Guerra, W. D.; Odella, E.; Urrutia, M. N.; Liddell, P. A.; Moore, T. A.; Moore, A. L. Models to Study Photoinduced Multiple Proton Coupled Electron Transfer Processes. *J. Porphyr. Phthalocyanines* **2021**, *25*, 674–682.

(2) Machan, C. W.; Sampson, M. D.; Chabolla, S. A.; Dang, T.; Kubiak, C. P. Developing a Mechanistic Understanding of Molecular Electrocatalysts for CO2 Reduction Using Infrared Spectroelectrochemistry. *Organometallics* **2014**, *33*, 4550–4559.

(3) Odella, E.; Wadsworth, B. L.; Mora, S. J.; Goings, J. J.; Huynh, M. T.; Gust, D.; Moore, T. A.; Moore, G. F.; Hammes-Schiffer, S.; Moore, A. L. Proton-Coupled Electron Transfer Drives Long-Range Proton Translocation in Bioinspired Systems. *J. Am. Chem. Soc.* **2019**, *141*, 14057–14061.

(4) Connelly, N. G.; Geiger, W. E. Chemical Redox Agents for Organometallic Chemistry. *Chem. Rev.* **1996**, *96*, 877–910.

(5) Oliver, T. A. A.; Lewis, N. H. C.; Fleming, G. R. Correlating the Motion of Electrons and Nuclei with Two-Dimensional Electronic–Vibrational Spectroscopy. *Proc. Natl. Acad. Sci. U. S. A.* **2014**, *111*, 10061–10066.

(6) Myers, J. A.; Lewis, K. L. M.; Tekavec, P. F.; Ogilvie, J. P. Two-Color Two-Dimensional Fourier Transform Electronic Spectroscopy with a Pulse-Shaper. *Opt. Express* **2008**, *16*, 17420–17428.

(7) Zhang, Z.; Wells, K. L.; Hyland, E. W. J.; Tan, H. S. Phase-Cycling Schemes for Pump-Probe Beam Geometry Two-Dimensional Electronic Spectroscopy. *Chem. Phys. Lett.* **2012**, *550*, 156–161.

(8) Wu, E. C.; Ge, Q.; Arsenault, E. A.; Lewis, N. H. C.; Gruenke, N. L.; Head-Gordon, M.; Fleming, G. R. Two-Dimensional Electronic-Vibrational Spectroscopic Study of Conical Intersection Dynamics: An Experimental and Electronic Structure Study. *Phys. Chem. Chem. Phys.* **2019**, *21*, 14153–14163.

(9) Lewis, N. H. C.; Dong, H.; Oliver, T. A. A.; Fleming, G. R. Measuring Correlated Electronic and Vibrational Spectral Dynamics Using Line Shapes in Two-Dimensional Electronic-Vibrational Spectroscopy. *J. Chem. Phys.* **2015**, *142*, 174202.

(10) Adamo, C.; Barone, V. Toward Reliable Density Functional Methods without Adjustable Parameters: The PBE0 Model. *J. Chem. Phys.* **1999**, *110*, 6158–6170.

(11) Runge, E.; Gross, E. K. U. Density-Functional Theory for Time-Dependent Systems. *Phys. Rev. Lett.* **1984**, *52*, 997–1000.

(12) Rohrdanz, M. A.; Martins, K. M.; Herbert, J. M. A Long-Range-Corrected Density Functional That Performs Well for Both Ground-State Properties and Time-Dependent Density Functional Theory Excitation Energies, Including Charge-Transfer Excited States. *J. Chem. Phys.* **2009**, *130*, 054112.

(13) Shee, J.; Head-Gordon, M. Predicting Excitation Energies of Twisted Intramolecular Charge-Transfer States with the Time-Dependent Density Functional Theory: Comparison with Experimental Measurements in the Gas Phase and Solvents Ranging from Hexanes to Acetonitrile. *J. Chem. Theory Comput.* **2020**, *16*, 6244–6255.

(14) Epifanovsky, E.; Gilbert, A. T. B.; Feng, X.; Lee, J.; Mao, Y.; Mardirossian, N.; Pokhilko, P.; White, A. F.; Coons, M. P.; Dempwolff, A. L.; Gan, Z.; Hait, D.; Horn, P. R.; Jacobson, L. D.; Kaliman, I.; Kussmann, J.; Lange, A. W.; Lao, K. U.; Levine, D. S.; Liu, J.; McKenzie, S. C.; Morrison, A. F.; Nanda, K. D.; Plasser, F.; Rehn, D. R.; Vidal, M. L.; You, Z. Q.; Zhu, Y.; Alam, B.; Albrecht, B. J.; Aldossary, A.; Alguire, E.; Andersen, J. H.; Athavale, V.; Barton, D.; Begam, K.; Behn, A.; Bellonzi, N.; Bernard, Y. A.; Berquist, E. J.; Burton, H. G. A.; Carreras, A.; Carter-Fenk, K.; Chakraborty, R.; Chien, A. D.; Closser, K. D.; Cofer-Shabica, V.; Dasgupta, S.; De Wergifosse, M.; Deng, J.; Diedenhofen, M.; Do, H.; Ehlert, S.; Fang, P. T.; Fatehi, S.; Feng, Q.; Friedhoff, T.; Gayvert, J.; Ge, Q.; Gidofalvi, G.; Goldey, M.; Gomes, J.; González-Espinoza, C. E.; Gulania, S.; Gunina, A. O.; Hanson-Heine, M. W. D.; Harbach, P. H. P.; Hauser, A.; Herbst, M. F.; Hernández Vera, M.; Hodecker, M.; Holden, Z. C.; Houck, S.; Huang, X.; Hui, K.; Huynh, B. C.; Ivanov, M.; Jász, Á.; Ji, H.; Jiang, H.; Kaduk, B.; Kähler, S.; Khistyaev, K.; Kim, J.; Kis, G.; Klunzinger, P.; Koczor-Benda, Z.; Koh, J. H.; Kosenkov, D.; Koulias, L.; Kowalczyk, T.; Krauter, C. M.; Kue, K.; Kunitsa, A.; Kus, T.; Ladjánszki, I.; Landau, A.; Lawler, K. V.; Lefrancois, D.; Lehtola, S.; Li, R. R.; Li, Y. P.; Liang, J.; Liebenthal, M.; Lin, H. H.; Lin, Y. S.; Liu, F.; Liu, K. Y.; Loipersberger, M.; Luenser, A.; Manjanath, A.; Manohar, P.; Mansoor, E.; Manzer, S. F.; Mao, S. P.; Marenich, A. V.; Markovich, T.; Mason, S.; Maurer, S. A.; McLaughlin, P. F.; Menger, M. F. S. J.; Mewes, J. M.; Mewes, S. A.; Morgante, P.; Mullinax, J. W.; Oosterbaan, K. J.; Paran, G.; Paul, A. C.; Paul, S. K.; Pavošević, F.; Pei, Z.; Prager, S.; Proynov, E. I.; Rák, Á.; Ramos-Cordoba, E.; Rana, B.; Rask, A. E.; Rettig, A.; Richard, R. M.; Rob, F.; Rossomme, E.; Scheele, T.; Scheurer, M.; Schneider, M.; Sergueev, N.; Sharada, S. M.; Skomorowski, W.; Small, D. W.; Stein, C. J.; Su, Y. C.;

Sundstrom, E. J.; Tao, Z.; Thirman, J.; Tornai, G. J.; Tsuchimochi, T.; Tubman, N. M.; Veccham, S. P.; Vydrov, O.; Wenzel, J.; Witte, J.; Yamada, A.; Yao, K.; Yeganeh, S.; Yost, S. R.; Zech, A.; Zhang, I. Y.; Zhang, X.; Zhang, Y.; Zuev, D.; Aspuru-Guzik, A.; Bell, A. T.; Besley, N. A.; Bravaya, K. B.; Brooks, B. R.; Casanova, D.; Chai, J. Da; Coriani, S.; Cramer, C. J.; Cserey, G.; Deprince, A. E.; Distasio, R. A.; Dreuw, A.; Dunietz, B. D.; Furlani, T. R.; Goddard, W. A.; Hammes-Schiffer, S.; Head-Gordon, T.; Hehre, W. J.; Hsu, C. P.; Jagau, T. C.; Jung, Y.; Klamt, A.; Kong, J.; Lambrecht, D. S.; Liang, W.; Mayhall, N. J.; McCurdy, C. W.; Neaton, J. B.; Ochsenfeld, C.; Parkhill, J. A.; Peverati, R.; Rassolov, V. A.; Shao, Y.; Slipchenko, L. V.; Stauch, T.; Steele, R. P.; Subotnik, J. E.; Thom, A. J. W.; Tkatchenko, A.; Truhlar, D. G.; Van Voorhis, T.; Wesolowski, T. A.; Whaley, K. B.; Woodcock, H. L.; Zimmerman, P. M.; Faraji, S.; Gill, P. M. W.; Head-Gordon, M.; Herbert, J. M.; Krylov, A. I. Software for the Frontiers of Quantum Chemistry: An Overview of Developments in the Q-Chem 5 Package. *J. Chem. Phys.* **2021**, *155*, 084801.

(15) Herbert, J. M. Dielectric Continuum Methods for Quantum Chemistry. *Wiley Interdiscip. Rev. Comput. Mol. Sci.* **2021**, *11*, e1519.

(16) Rehm, D.; Weller, A. Kinetics of Fluorescence Quenching by Electron and H-Atom Transfer. *Isr. J. Chem.* **1970**, *8*, 259–271.

(17) Weller, A. Photoinduced Electron Transfer in Solution: Exciplex and Radical Ion Pair Formation Free Enthalpies and Their Solvent Dependence. *Zeitschrift für Phys. Chemie* **1982**, *133*, 93–98.

(18) Guerra, W. D.; Odella, E.; Secor, M.; Goings, J. J.; Urrutia, M. N.; Wadsworth, B. L.; Gervaldo, M.; Sereno, L. E.; Moore, T. A.; Moore, G. F.; Hammes-Schiffer, S.; Moore, A. L. Role of Intact Hydrogen-Bond Networks in Multiproton-Coupled Electron Transfer. *J. Am. Chem. Soc.* **2020**, *142*, 21842–21851.

(19) Rumble, J. R. ed. *Handbook of Chemistry and Physics 100th Edition*; 2019.

(20) Yoneda, Y.; Mora, S. J.; Shee, J.; Wadsworth, B. L.; Arsenault, E. A.; Hait, D.; Kodis, G.; Gust, D.; Moore, G. F.; Moore, A. L.; Head-Gordon, M.; Moore, T. A.; Fleming, G. R. Electron–Nuclear Dynamics Accompanying Proton-Coupled Electron Transfer. *J. Am. Chem. Soc.* **2021**, *143*, 3104–3112.

(21) Martin, R. L. Natural Transition Orbitals. *J. Chem. Phys.* **2003**, *118*, 4775.